



Predicting flow curves of two-phase steels from spherical nanoindentation data of constituent phases: Isostrain method vs. non-isostrain method

Moo-Young Seok, Yong-Jae Kim, In-Chul Choi, Yakai Zhao, Jae-il Jang*

Division of Materials Science and Engineering, Hanyang University, Seoul 133-791, Republic of Korea

ARTICLE INFO

Article history:

Received 2 November 2013

Received in final revised form 31 January 2014

Available online 26 March 2014

Keywords:

Flow curves

Two-phase alloy

Nanoindentation

Constituent phase

ABSTRACT

A procedure is suggested to predict the flow curves of two-phase steels using data from nanoindentation experiments performed with two spherical indenters having different radii. The procedure incorporates two steps: First, the “macroscopic” (or size effect corrected) stress–strain relations of each constituent phase are estimated based on the concepts of indentation stress/strain and indentation size effect. Then, the “overall” (or composite) flow curve of two-phase steel is extracted in two different ways; an isostrain method (ISM) and a non-isostrain method (NISM). The appropriateness of the proposed procedure was examined by performing a series of spherical nanoindentation tests on various two-phase steels (consisting of ferrite–pearlite or ferrite–bainite). Reasonable accuracy of the prediction was validated by comparing the predicted curves to the tensile curves obtained from standard tests of bulky samples. In addition, interestingly, the predictions made by the simple ISM were almost identical to those by the more sophisticated NISM, though the NISM used more realistic assumptions.

© 2014 Elsevier Ltd. All rights reserved.

1. Introduction

In the development of advanced structural alloys, controlling their microstructure is undoubtedly the most important aspect to optimize mechanical performance. Extensive research has been performed to establish proper models for predicting microstructures from chemical compositions and processing conditions, and now some models are practically applied in the industrial fields (especially, steel industries). However, despite significant effort, there is no established way to precisely predict the final mechanical properties from microstructural features.

Most previous research on the prediction of mechanical properties (Asgari et al., 2009; Choi et al., 2009a; Hüper et al., 1999; Ishikawa et al., 2000, 2006a,b; Karlsson and Linden, 1975; Khan et al., 2012; Kim and Thomas, 1981; Koo et al., 1980; Lanzillotto and Pickering, 1982; Ramazani et al., 2012, 2013a,b; Rudiono and Tomota, 1997; Sun and Wagoner, 2013; Tomota et al., 1976, 1992; Zhu and Lu, 2012) has targeted the development of a proper model for the alloys consisting of the two-phase microstructure that is common in many commercial-grade steels. It is well accepted that the nature of plastic flow behavior in two-phase steels depends on the mechanical properties of each phase and the volume fractions of the phases in many different ways (Choi et al., 2009a; Kim and Thomas, 1981; Koo et al., 1980; Lanzillotto and Pickering, 1982). Therefore, in developing a prediction method for designing two-phase steels and optimizing their flow

* Corresponding author. Tel.: +82 222200402; fax: +82 222202294.

E-mail address: jjjang@hanyang.ac.kr (J.-i. Jang).

properties, both the properties and fractions of the phases and the way how they affect the overall flow curve should be carefully taken into consideration.

While one of the simplest approaches for predicting the flow curve of two-phase steel is a method based on the assumption of equal strain in each phase (hereinafter called “isostrain method”, ISM), there is a more sophisticated method that assumes different strain in each phase (hereinafter referred to as “non-isostrain method”, NISM). One of the most popular NISMs was suggested in the middle of 1970s by Tomota and colleagues (Rudiono and Tomota, 1997; Tomota et al., 1976, 1992) who designed a micromechanical way on the basis of Eshelby’s inclusion theory (Eshelby, 1957) and Mori–Tanaka mean field concept (Mori and Tanaka, 1973). Ishikawa and colleagues (Hüper et al., 1999; Ishikawa et al., 2000, 2006a,b) adopted Tomota’s NISM to optimize the volume fractions of the phases in high-strength dual-phase steels. However, a fundamental difficulty remains in previous ISM and NISM; although the flow curves of each phase are essentially required for both methods, standard tensile/compression tests cannot be performed on such a small volume of micro-phase. One promising technique to overcome this difficulty is nanoindentation (Oliver and Pharr, 1992, 2004) which has been widely used to probe local mechanical properties in crystalline/amorphous metals (for instance, Choi et al., 2009b; Chollacoop and Ramamurty, 2005, 2006; Jang et al., 2007; Moon et al., 2008; Oh et al., 2011; Yoo et al., 2009) because the technique requires only a small volume of target material. While three-sided pyramidal indenters (especially, Berkovich indenter having a centerline-to-face angle of 65.3°) have been popularly adopted for the technique, nanoindentation with a spherical indenter provides distinct merits (Choi et al., 2009a, 2011; Jang et al., 2005; Johnson, 1985; Kang et al., 2013; Tabor, 1951; Yoo et al., 2010) based on the fact that stresses and strains beneath the contact increase as penetration depth (and load) increases. With continuum mechanics viewpoints, similar behavior does not occur during a sharp indentation due to the tip’s geometrical self-similarity.

In the present study, we suggest a procedure for predicting the overall flow curves of two-phase steel from nanoindentation data obtained with two spherical indenters having different radii. Two different methods, including ISM and NISM, were used for the predictions, and the difference in their results was investigated. The appropriateness of the proposed procedure was examined by comparing the predictions to the experimental data obtained from standard tensile tests of bulky samples. Before starting, it is noteworthy that, here, the term “two-phase” indicates two different microstructures such as ferrite vs. pearlite or ferrite vs. bainite. Although pearlite and bainite are not truly “phases” but “specific microstructures”, (Rudiono and Tomota, 1997) they are treated as phases in the present study for the sake of simplicity.

2. Experimental

The two-phase steels examined in this study were three low-carbon steels and an API X100 linepipe steel. The low-carbon steels having compositions (in wt%) of Fe–X%C–1.2Mn–0.15Si (with $X = 0.04, 0.07, \text{ and } 0.10$) were heated up to 1000 °C for 600 s and then cooled down to room temperature at 1 °C/s using a thermo-mechanical simulator Gleeble 1500 (Dynamic Systems Inc., Poestenkill, NY) in order to obtain two-phase microstructures of ferrite and pearlite. The API X100 steel consisting of ferrite–bainite microstructures was a commercial-grade high-strength steel having a nominal composition of Fe–(0.05–0.07)C–0.25Si–2.0Mn–0.01P–0.001S–0.05Nb–0.05V–0.3Mo (in wt%).

All specimens were mechanically polished with fine SiC paper with grit number of up to 2000, then electrolytically polished using a Lectropol-5 instrument (Struers, Westlake, OH) in a solution (ethanol 80%, distilled water 14%, perchloric acid 6%) to avoid artifacts related to a hardened surface layer possibly introduced during grinding. Specimens were etched with 3% Nital solution for microstructure observations by an optical microscope (Olympus, Tokyo, Japan). The grain size and volume fraction of each phase were measured by an image analyzer, Image-Pro (Media Cybernetics Inc., Silver Springs, MD).

Nanoindentation tests were carried out using a Nanoindenter-XP (formerly MTS; now Agilent Technologies, Oak Ridge, TN) with two spherical diamond indenters having different radii. The real (or “effective”) tip radius R was determined by analyzing data from the indentations made on a fused quartz sample based on Hertzian contact theory (Johnson, 1985). Load-controlled indentations were performed at a peak load P_{\max} of 15 mN under a constant indentation strain rate (dP/dt)/ P (where P is the indentation load) of 0.05/s. After indentation, the specimens were slightly etched in 3% Nital acid for examining whether or not the indentation was made inside the target phase in a field-emission SEM, JSM-6330F (JEOL Ltd., Tokyo, Japan). Finally, for comparison purposes, the uniaxial stress–strain curves were obtained through standard tensile tests that were conducted using a universal testing machine, Z100 (Zwick GmbH & Co., Ulm, Germany).

3. Procedure for predicting the flow curve of two-phase steel

3.1. Estimating macroscopic flow curves of constituent phases

The procedure suggested here for predicting the flow curve of two-phase steel incorporates two steps; (1) experimental estimation of the “macroscopic” flow curves of each constituent phase through spherical nanoindentations, and (2) theoretical extraction of the “overall” (or composite) flow curve of two-phase steel from the curves of each phase.

The main part of the first step is to convert the spherical nanoindentation data to the macroscopic stress–strain curve of each phase. Note that the macroscopic curve means the size effect corrected curve that can be directly compared to the curve obtained from the standard tensile test on a bulky sample. It is well accepted (e.g., see Cao and Lu, 2004; Herbert et al., 2006;

Jang et al., 2005; Sreeranganathan et al., 2008) that the representative flow stress $\sigma_{f,ind}$ (meaning the indentation stress at a characteristic strain ε_{charac}) can be determined by the well-known Tabor's empirical relationship, $\sigma_{f,ind} = \frac{H}{C} = \frac{P}{\pi a^2 C}$, where H is the hardness (that is equal to the mean contact pressure p_m), C is the constraint factor (~ 3 for fully plastic deformation (Shim et al., 2008)), P is the indentation load, and a is the contact radius. The characteristic strain underneath a spherical indenter is often described as $\varepsilon_{charac} = 0.2 \frac{a}{R}$ where R is the effective radius of the spherical tip (Tabor, 1951). Therefore, $\sigma_{f,ind}$ and ε_{charac} can be determined when the value of a is calculated by putting the contact depth h_c (given by $h_c = h - \omega \frac{S}{\sigma}$ (Oliver and Pharr, 1992, 2004) where S is the contact stiffness and ω is a geometric constant of 0.75 for a sphere) into the contact geometry equation $a^2 = 2Rh_c - h_c^2$ (Choi et al., 2009a).

Since the nanoindentation hardness H is known to exhibit so-called indentation size effect (ISE), extreme care must be taken in converting the H data to size effect corrected values. For spherical indentation, a strong dependency of H (and thus σ) on the R has been reported (Lim and Chaudhri, 1999; Shim et al., 2008; Swadener et al., 2002), that is, a smaller R results in a higher H . In a somewhat analogous way to the popular ISE model for sharp indentation (so-called Nix–Gao model (Nix and Gao, 1998)), Swadener et al. (2002) experimentally verified that the ISE for spherical indentation can be described as:

$$H = H_0 \sqrt{1 + \frac{R^*}{R}} \quad (1)$$

where H_0 is the macroscopic hardness and R^* is a material length scale for the R dependence of H . In this equation, H and H_0 can be simply replaced by σ and σ_0 (the macroscopic strength) according to $H \sim 3\sigma$. Finally, from the calculated “macroscopic” flow stress and characteristic strain, the relation of true stress vs. true strain for each phase is described by the simple power-law-type Hollomon equation (Hollomon, 1945):

$$\sigma = K \varepsilon^n \quad (2)$$

where K is the strength coefficient and n is the work-hardening exponent. In this procedure, special caution is required when using this equation. The strain ε in Eq. (2) is not the plastic strain but the total strain, and Eq. (2) is applied to the regime where the total strain is equal to or larger than the yield strain. Thus, below the yield strain (that may be determined as the crossing point of the curve of Eq. (2) and the line of Hooke's law), the constitutive relation is assumed to follow Hooke's law (with $E = 200$ GPa for steels).

3.2. Extracting the overall flow curve of two-phase steel from the phase curves

In the present study, two different methods, including ISM and NISM, are adopted to extract the “overall” flow curves of two-phase steels from the curves of each phase. First, in ISM (see Fig. 1a) which is less realistic but much simpler than NISM, the plastic strain of the softer phase A is assumed to be the same as that of the harder phase B. Thus, at a given strain, the overall stress (i.e., composite stress) of the two-phase steel consisting of phases A and B can be predicted by applying a simple rule-of-mixture:

$$\sigma_C = \sigma_A f_A + \sigma_B f_B \quad (3)$$

where f is the volume fraction, and subscripts C, A, and B indicate composite, phase A, and phase B, respectively.

The NISM suggested here is modified from the micromechanical model of Tomota and colleagues (Rudiono and Tomota, 1997; Tomota et al., 1976, 1992) who assumed that, due to the mutual constraint, each phase of the two-phase steel undergoes a different level of strain during deformation. Tomota's analysis is based on the constitutive relationship between the stress σ and plastic strain ε_p that was originally a linear hardening relation $\sigma = \sigma_y + \chi \varepsilon_p$ (where σ_y is the yield strength and χ is the strain hardening rate or the slope of the strain hardening) (Tomota et al., 1976), and later, the Swift equation (Swift, 1952; Tomota et al., 1992) $\sigma = \alpha(\beta + \varepsilon_p)^n$ (where α and β are constants and n is the work-hardening exponent). However, it should be noted that while ε_p in the Swift equation is defined as the total strain minus yield strain ($\varepsilon_t - \varepsilon_y$), the value of ε_p in Tomota's analysis is given as $(\varepsilon_t - \varepsilon_e)$ where ε_e is the elastic strain (equivalent to σ/E ; see Fig. 1b). To avoid this confusion, here we adopt the Hollomon equation (Eq. (2)) instead of the Swift equation and accordingly modify Tomota's analysis to the ε_p -based format that can be directly applied to Eq. (2).

Fig. 1c exhibits a schematic of the NISM used in this study, wherein deformation of the two-phase composite is divided into three stages. In Stage I, both the softer phase A and the harder phase B deform elastically and have almost the same elastic modulus E (which is a reasonable assumption for iron and steels in which typically $E \sim 200$ GPa). When an applied stress σ reaches the yield strength of phase A, $(\sigma_y)_A$ in Fig. 1c, Stage II starts. In Stage II, phase A deforms plastically, whereas phase B continues to deform elastically, indicating that the overall yield strength of the two-phase composite is equal to $(\sigma_y)_A$. Thus, if the same external stresses are applied, the phase A experiences a larger strain, resulting in strain mismatch at the inter-phase boundaries that may follow original Eshelby model (Eshelby, 1957). As the plastic deformation of phase A proceeds with increasing applied stresses, the strain mismatch must increase. The mismatch increase induces a non-negligible level of internal stress that can depress further plastic flow in phase A and, at the same time, can make the yielding of phase B occur at a stress lower than its own yield strength, $(\sigma_y)_B$ in Fig. 1c. Therefore, the overall stress σ_C in Stage II can be described as the sum of the flow stress of phase A and the internal stress that is determined by the misfit strain and volume fraction f_B (Tomota et al., 1976):

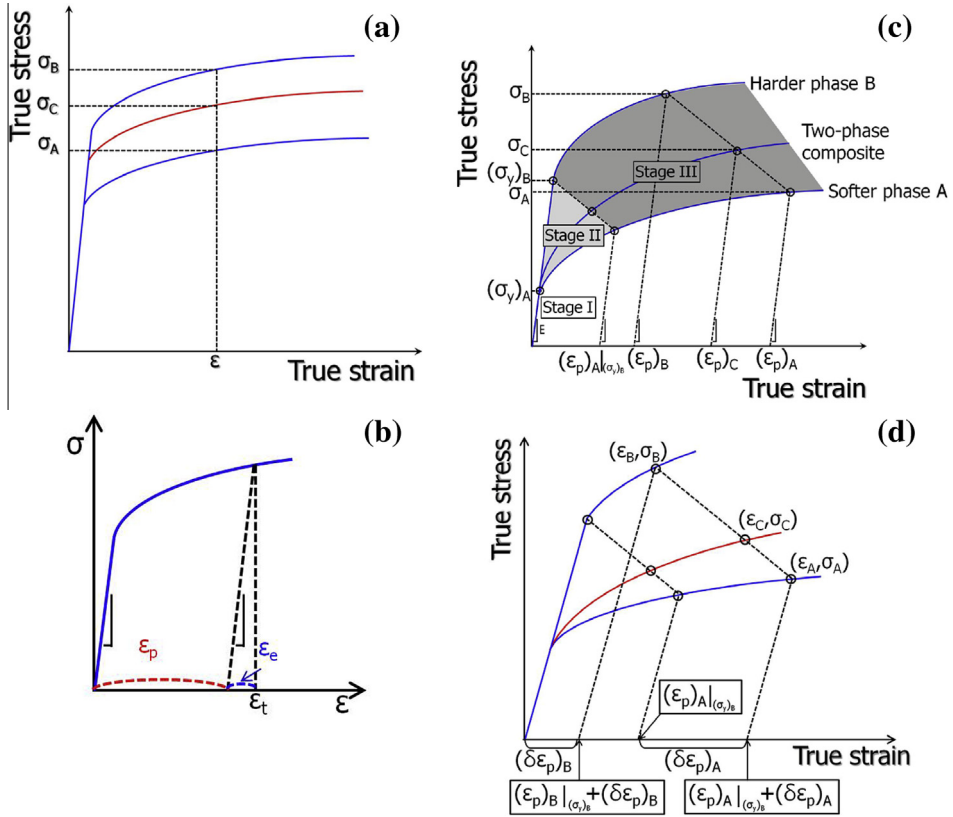


Fig. 1. Schematic illustrations of (a) isostrain method (ISM); (b) elastic strain and the plastic strain; (c) non-isostrain method (NISM); (d) misfit strain in Stage III of NISM.

$$\sigma_C = \sigma_A|_{\epsilon_A} + f_B \cdot \theta \cdot \left(\epsilon_A - \frac{\sigma_A}{E} \right) \quad (4)$$

where ϵ_A is the total strain of phase A, $\sigma_A|_{\epsilon_A}$ is the flow stress of phase A at ϵ_A , and θ is a material constant that is, according to Eshelby (1957), $E(7 - 5\nu)/\{10(1 - \nu^2)\}$ in the case of spherical grains where E and ν are Young's modulus and Poisson's ratio, respectively.

The total strain ϵ (Eq. (2)) of the composite in Stage II is sum of the elastic strain ϵ_e and the plastic strain ϵ_p (see Fig. 1b):

$$\epsilon_C = (\epsilon_e)_C + (\epsilon_p)_C = \frac{\sigma_C}{E} + (\epsilon_p)_C. \quad (5)$$

Here, the plastic strain of the composite $(\epsilon_p)_C$ can be given as $(1 - f_B) \cdot (\epsilon_p)_A + f_B \cdot (\epsilon_p)_B$ and, in Stage II, is equal to $(1 - f_B) \cdot (\epsilon_p)_A$ since $(\epsilon_p)_B = 0$ (Tomota et al., 1976).

In Stage III, both phase A and B deform plastically. This stage starts at the onset of the plastic flow of the harder phase B. At an applied stress of $\sigma_A|_{\epsilon_A @ (\sigma_y)_B}$, the internal stress (accumulated in phase B in Stage II) added to the applied stress allows phase B to begin plastic deformation. The plastic strain of phase A at the onset of Stage III (i.e., at the yielding of phase B) $\epsilon_A|_{(\sigma_y)_B}$ can be determined by the following simultaneous equations that are based on the flow stresses of A and B, respectively.

$$\sigma_C = \sigma_A|_{\epsilon_A @ (\sigma_y)_B} + f_B \cdot \theta \cdot \left(\epsilon_A - \frac{\sigma_A}{E} \right) \Big|_{(\sigma_y)_B} \quad (6)$$

$$\sigma_C = (\sigma_y)_B - (1 - f_B) \cdot \theta \cdot \left(\epsilon_A - \frac{\sigma_A}{E} \right) \Big|_{(\sigma_y)_B}. \quad (7)$$

Similar to Eq. (4), the first and second terms of these equations correspond to the flow stress and internal stress, respectively.

While both phases undergo plastic deformation during Stage III, the misfit strain at the inter-phase boundary $\Delta\epsilon_p$ can be described as a function of the small increase in plastic strain of each phase, $(\delta\epsilon_p)_A$ and $(\delta\epsilon_p)_B$ (see Fig. 1d):

$$\Delta\epsilon_p = \left\{ (\epsilon_p)_A|_{(\sigma_y)_B} + (\delta\epsilon_p)_A \right\} - \left\{ (\epsilon_p)_B|_{(\sigma_y)_B} + (\delta\epsilon_p)_B \right\} \quad (8)$$

where $(\varepsilon_p)_B|_{(\sigma_y)_B}$ is the plastic strain of phase B at the phase's yielding and is thus zero. Since ε of Eq. (2) is not the plastic strain but the total strain, Eq. (8) should be described in terms of the total strain. If the right-hand term of Eq. (8) is reformulated according to Eq. (5) (see Fig. 1d), Eq. (8) can be rewritten as:

$$\Delta\varepsilon_p = \left(\varepsilon_A - \frac{\sigma_A|_{\varepsilon_A}}{E} \right) - \left(\varepsilon_B - \frac{\sigma_B|_{\varepsilon_B}}{E} \right). \quad (9)$$

With the misfit strain, the composite stress σ_C in Stage III can be calculated by solving the following simultaneous equations:

$$\sigma_C = \sigma_A|_{\varepsilon_A} + f_B \cdot \theta \cdot \Delta\varepsilon_p \quad (10)$$

$$\sigma_C = \sigma_B|_{\varepsilon_B} - (1 - f_B) \cdot \theta \cdot \Delta\varepsilon_p \quad (11)$$

and thus,

$$\sigma_A|_{\varepsilon_A} - \sigma_B|_{\varepsilon_B} + \theta \cdot \Delta\varepsilon_p = 0. \quad (12)$$

From Eqs. (9) and (12),

$$\sigma_A|_{\varepsilon_A} - \sigma_B|_{\varepsilon_B} + \theta \cdot \left[\left\{ \varepsilon_A - \frac{\sigma_A|_{\varepsilon_A}}{E} \right\} - \left\{ \varepsilon_B - \frac{\sigma_B|_{\varepsilon_B}}{E} \right\} \right] = 0. \quad (13)$$

Hence,

$$\left(\sigma_B|_{\varepsilon_B} - \sigma_A|_{\varepsilon_A} \right) \left(\frac{\theta}{E} - 1 \right) + \theta \cdot (\varepsilon_A - \varepsilon_B) = 0 \quad (14)$$

that can be re-described as

$$\left(K_B \varepsilon_B^{n_B} - K_A \varepsilon_A^{n_A} \right) \left(\frac{\theta}{E} - 1 \right) + \theta \cdot (\varepsilon_A - \varepsilon_B) = 0. \quad (15)$$

Here, K , n , θ , E are known, and ε_A and ε_B are unknown. By putting an arbitrary value of ε_A into Eq. (15), ε_B can be calculated. Then, one can estimate the evolution of σ_C by applying various sets of ε_A and ε_B to either Eq. (10) or (11).

On the other hand, the total strain in Stage III can be simply determined by Eq. (5). The plastic strain of Eq. (5) (see Fig. 1c) is given as:

$$(\varepsilon_p)_C = (\varepsilon_p)_C|_{(\sigma_y)_B} + (\delta\varepsilon_p)_C \quad (16)$$

where

$$(\delta\varepsilon_p)_C = (1 - f_B) \cdot (\delta\varepsilon_p)_A + f_B \cdot (\delta\varepsilon_p)_B. \quad (17)$$

Conclusively, by putting σ_C and ε_C , calculated according to Eqs. (10) [or (11)] and (5), into the Hollomon equation (Eq. (2)), the flow curve of a two-phase steel can be predicted.

4. Experimental verification of the suggested procedure

4.1. Ferrite-pearlite steels having different carbon contents

The first application of the proposed procedure was made to three low-carbon steels having different carbon contents. Fig. 2 shows the representative microstructures consisting of ferrite and pearlite (white and dark, respectively, in the images). The size and volume fraction of each phase are summarized in Table 1, which shows that the size and fraction of pearlite increase and those of ferrite decrease with increasing carbon content. Note that the size of pearlite does not indicate grain size, but represents the colony size of its ferrite-cementite system. The colony size was considered as the size of dark region in Fig. 2.

Nanoindentation tests were performed with two spherical tips having different radii (2.84 and 5.73 μm). Since intentionally conducting indentation on the target phase was impossible due to the electro-polished mirror surfaces, slight etching was conducted after indentation, making it possible to determine which indentations were made near the center of the target phase (see inset SEM images of Fig. 3) and thus to exclude (or, at least, minimize) the influences of the grain boundaries. Fig. 3 shows typical load-displacement (P - h) curves obtained from indentations on each phase. Ferrite exhibits a larger peak-load displacement h_{max} than pearlite, implying that the latter has a higher H than the former. Fig. 4a summarizes the variations in H for each phase with normalized displacement h/h_{max} . It should be noted that the data points at the very early stage of contact were not used due to their somewhat large fluctuations. Three trends are evident in Fig. 4a: First, for both tips, H increases with indentation depth. Second, as expected from Fig. 3, pearlite exhibits higher H than ferrite. Last but not least, H values for smaller R (2.84 μm) are much higher than those for larger R (5.73 μm). From the data in Fig. 4a, the plots of representative stress vs. characteristic strain were obtained according to the suggested procedure as shown in

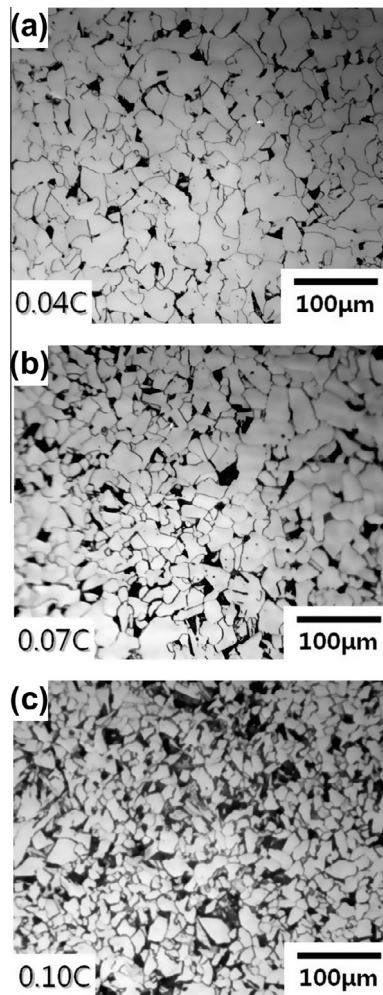


Fig. 2. Optical micrographs showing typical microstructures of the low-carbon steels; (a) 0.04 C, (b) 0.07 C, and (c) 0.10 C.

Table 1

Grain size and volume fraction of the low-carbon steels.

Carbon content	Ferrite		Pearlite	
	Grain size (μm)	Volume fraction (%)	Colony size (μm)	Volume fraction (%)
0.04 C	17.10 ± 9.35	95.79	13.09 ± 3.40	4.21
0.07 C	14.70 ± 8.43	90.17	14.14 ± 6.35	9.83
0.10 C	10.81 ± 6.02	71.60	18.66 ± 12.32	28.40

Fig. 4b. Somewhat interestingly, in the figure (and also in Fig. 4a), the flow curves of each phase are almost independent of carbon content. This may be explained by the limited solubility of carbon in the ferrite matrix (e.g., 0.008 wt% according to the equilibrium Fe–C phase diagram). Since additional carbon content over the solubility limit cannot be accommodated into the ferrite matrix (and only increases the volume fraction of pearlite, as listed in Table 1), the contribution of carbon's solid solution strengthening to the matrix strength is expected to be almost the same in the steels. A similar carbon-content-independence of H in ferrite has been reported in the literature (Davis, 1998; Lobo and Geiger, 1976; Moon et al., 2008).

By extrapolating the stress data in Fig. 4b to a reasonably large radius ($R = 500 \mu\text{m}$ (Choi et al., 2009a)) according to Eq. (1), the macroscopic flow curves of each phase were derived as exhibited in Fig. 5 in which the line for Hooke's law (with $E = 200 \text{ GPa}$) is also drawn. The macroscopic curves obtained for ferrite and pearlite are $\sigma_{\text{ferrite}} = 636 \cdot \varepsilon^{0.1936}$ and $\sigma_{\text{pearlite}} = 1692 \cdot \varepsilon^{0.2674}$, respectively. Finally, the overall flow curves of the three low-carbon steels were predicted using two different methods, ISM and NISM. Fig. 6 shows representative examples of the predicted curves (for 0.10 C steel). For clarity, low strain regimes (in which the differences in results between ISM and NISM are largest) are magnified in the inset images.

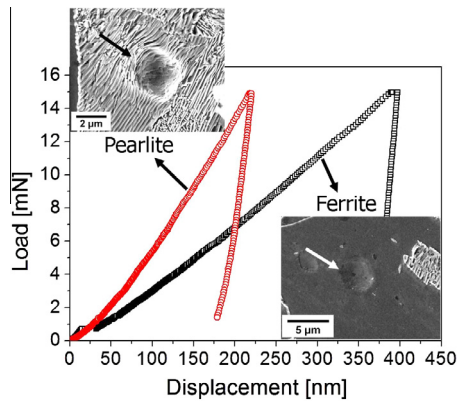


Fig. 3. Representative example of the P - h curves recorded during nanoindentation tests on each phase (for $R = 2.84 \mu\text{m}$). Inset SEM images show the hardness impressions made near the center of a grain.

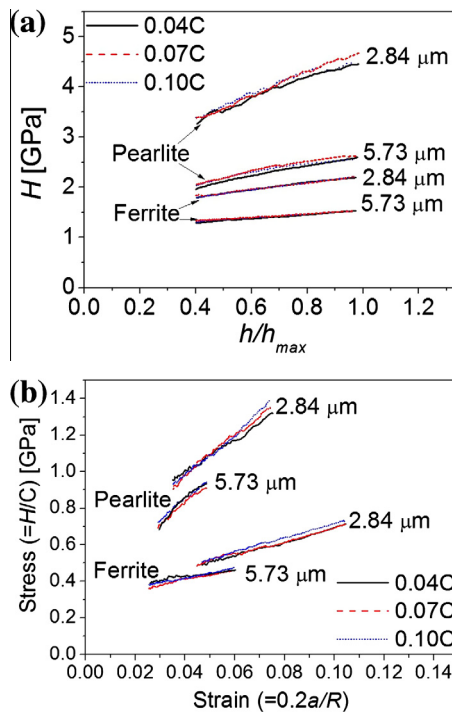


Fig. 4. Nanoindentation data of each phase; (a) plot of hardness vs. normalized indentation depth; (b) stress-strain relations converted from (a).

Fig. 7a compares the overall flow curves predicted by ISM to those predicted by NISM. The increase in flow stress with carbon content is due to the increase in pearlite fraction rather than the change in phase properties (see [Table 1](#)). The most interesting feature in **Fig. 7a** is that the predictions made by the simple ISM are very close to those made by the NISM. There are two possible reasons for this. On one hand, the difference between the predictions of the two methods is most significant in Stage II, that is, in the small deformation regime. In ductile alloys showing large elongation (such as the steels examined here), the portion of Stage II may be too small to affect the overall flow curve. On the other hand, in Stage III, NISM takes into account the misfit strain $\Delta\epsilon_p$ from Eq. (8). Since, in the steels, $(\delta\epsilon_p)_A$ and $(\delta\epsilon_p)_B$ of Eq. (8) are almost the same, the misfit strain effect in Stage III can be almost negligible, leading to nearly identical flow stresses during Stage III in both methods. This insignificant difference suggests that, for predicting the overall flow curves of two-phase steels with similar-level accuracies, one may better adopt the simple ISM instead of the more sophisticated NISM (at least, for the steels examined in this study) though the assumption of NISM is more realistic.

Fig. 7b shows the plots of true stress vs. true strain measured from the standard tensile tests. Although it is somewhat difficult to directly compare the predictions (**Fig. 7a**) to the experimental data (**Fig. 7b**) due to the pronounced Lüders

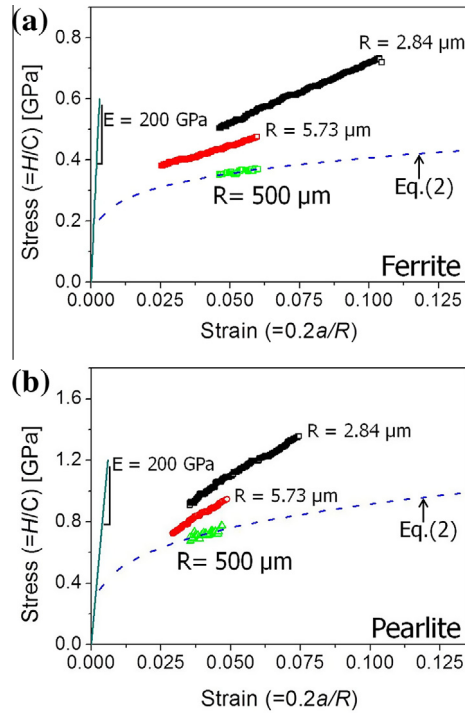


Fig. 5. Estimating the macroscopic stress–strain behavior of each phase; (a) ferrite; (b) pearlite.

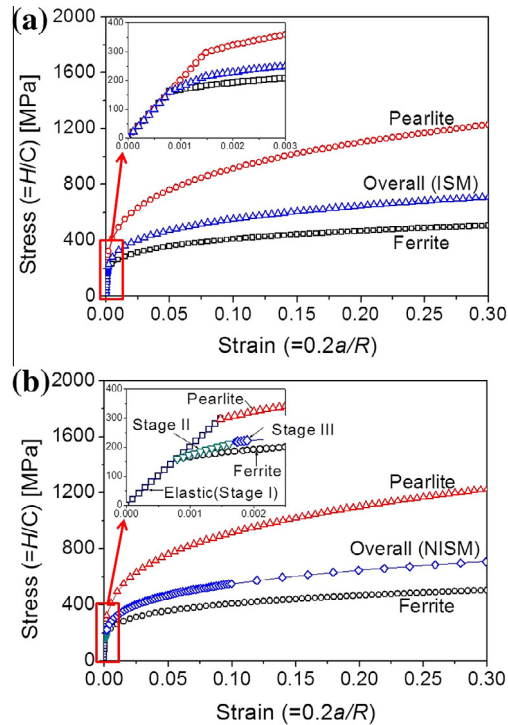


Fig. 6. Typical example (for 0.10 C steel) of the predicted overall flow curves from the curves of each phase; (a) ISM; (b) NISM. Low strain regime is magnified in the insets for clarity.

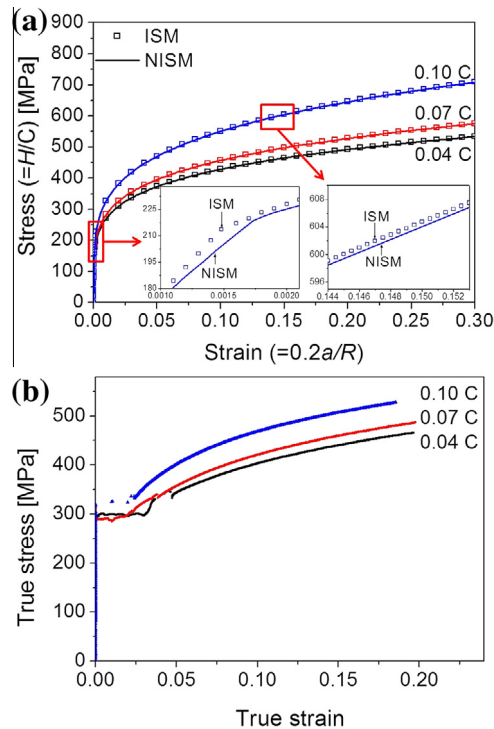


Fig. 7. Plots of true stress vs. true strain of the low-carbon steels; (a) comparison of the curves predicted by ISM and NISM; (b) flow curves from standard tensile tests.

elongation of the tensile curves, the comparison results in Table 2 provide some clues for understanding the appropriateness of the proposed procedure. At a given total strain (e.g., $\varepsilon = 0.1$ in Table 2), the flow stresses of the predicted curves are in a reasonable agreement with the experimental data. Relatively lower values in the experimental curves than the predictions may be because, in the experiments, the power-law relation following Eq. (2) is shifted to a higher strain regime due to the existence of Lüders elongation. More interestingly, in Table 2, the values of the work-hardening exponent, n of Eq. (2), from the tensile tests are very close to the predictions, as can be expected from the similar curve shapes in Figs. 7a and b. Since the absolute values of n must not be influenced by Lüders behavior, this good agreement suggests that the proposed procedure can determine the work hardenability of two-phase alloys with high accuracy.

4.2. Ferrite–bainite steel without Lüders elongation

As noted above, pronounced Lüders elongation can make it difficult to directly compare predictions to experimental data. In this regard, the proposed procedure was applied a second time to a two-phase steel that does not show Lüders elongation; API X100 steel with a microstructure composed of ferrite and bainite (having average size of 2.25 ± 1.82 and $2.06 \pm 1.56 \mu\text{m}$, respectively). Hüper et al. (1999) reported that the increase in the fraction of harder phase suppresses Lüders elongation of a two-phase steel, and hence Lüders behavior is rarely seen in steels having a bainite fraction larger than 30%. Since the average volume fractions of ferrite and bainite in the examined API steel are approximately 41% and 59%, respectively (Choi et al., 2009a), Lüders elongation in this steel is less pronounced vis-à-vis those in the low-carbon steels.

Fig. 8a shows the flow curves of each phase estimated according to the suggested procedure. The nanoindentation data were obtained from our group's previous study (Choi et al., 2009a) in which two indenters having different radii (550 nm and 3.3 μm) were used. According to the proposed procedure, the macroscopic stress–strain curves of the ferrite and bainite were determined to be $\sigma_{\text{ferrite}} = 957 \cdot \varepsilon^{0.2127}$ and $\sigma_{\text{bainite}} = 1418 \cdot \varepsilon^{0.0918}$, respectively. Note that the difference in the K value [in Eq. (2)] of ferrite phase between the two examined steels (636 MPa for the case of a low-carbon steel and 957 MPa for API X100

Table 2

Comparison of the predicted values and the experimental data.

Carbon Content	Work-hardening exponent, n			Flow stress [MPa] at $\varepsilon = 0.1$		
	ISM	NISM	Tensile test	ISM	NISM	Tensile test
0.04 C	0.2002	0.2003	0.2245	428.6	428.5	403.2
0.07 C	0.2080	0.2083	0.2318	457.1	456.8	420.8
0.10 C	0.2282	0.2288	0.2088	551.2	550.6	468.6

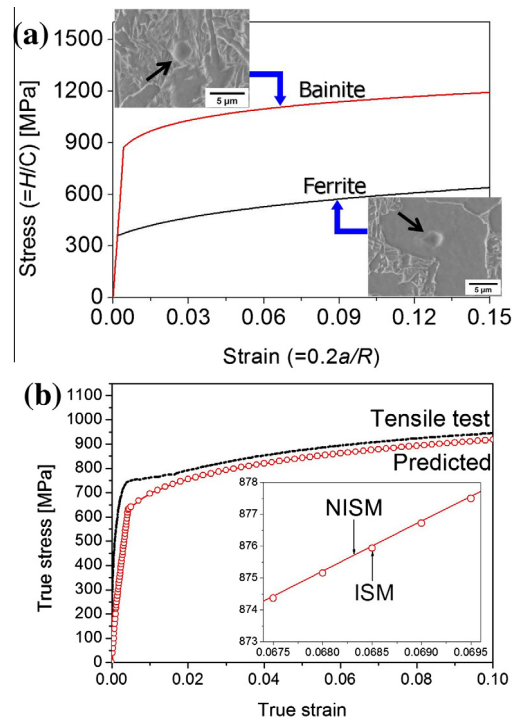


Fig. 8. Representative results of API X-100 steel; (a) macroscopic flow curves of each phase (with insets showing indentation locations); (b) comparison of the predicted curve to the experimental curve.

steel) can be easily explained by their different chemical compositions and thus different level of solid solution (and precipitate) strengthening effects.

The overall flow curves predicted by ISM and NISM are displayed in Fig. 8b where the tensile curve is also provided for comparison purpose. As in the case of low-carbon steels, there is almost no difference in the predictions of ISM and NISM (see the inset of Fig. 8b). In addition, reasonably good agreement is observed between the predicted curve and the uniaxial tensile curve (except for the small strain regime where a Lüders-like plateau exists). The work-hardening exponent n (in Eq. (2)) from the tensile tests ($n = 0.11126$) is very close to that of the predicted curve ($n = 0.1216$). This confirms that the strain hardening behavior of the two-phase alloy can be successfully predicted by the proposed procedure.

In Fig. 8b, the experimentally measured curve shows a slightly higher stress (~ 30 MPa) than the predicted curve, which may be primarily because grain (or inter-phase) boundary strengthening (which should be more significant for the finer API steel than for the low-carbon steels) is not considered in the procedure. Another possible reason for the slight difference is the fact that only two indenters were used. Using only two indenters always induces a linear relation between σ (or H) and R^2 (in Eq. (1)) in a deterministic way so that the extrapolated macroscopic strength can be significantly affected by a small fluctuation in σ (or H). Thus, the use of more indenters having different radii will certainly enhance the accuracy of the predictions. Note that, in the low-carbon steels (Fig. 7 and Table 2), a trend opposite to that in Fig. 8 is observed, i.e., the tensile flow stresses at a given strain are slightly lower than the predicted values. As mentioned earlier, this is simply because the experimentally obtained curve is shifted to a higher strain regime by Lüders elongation.

5. Conclusion

A procedure has been proposed to predict the overall (or composite) flow curve of two-phase steel from the spherical nanoindentation data for each constituent phase. The concepts of indentation stress/strain and indentation size effect are used to estimate the macroscopic flow curves of each phase. Using the phase curves, the overall flow curve of a two-phase steel (ferrite–pearlite or ferrite–bainite) was extracted with two different methods: ISM and NISM. The results revealed that the proposed procedure can successfully predict the plastic flow of two-phase steel. Interestingly, the predictions made by simple ISM were almost identical to those made by the more complex NISM, though NISM used more realistic assumptions.

Acknowledgements

This work was supported in part by the National Research Foundation of Korea (NRF) grant funded by the Korea government (MSIP) (No. 2013R1A1A2A10058551), and in part by the Human Resources Development program of the Korea Insti-

tute of Energy Technology Evaluation and Planning (KETEP) grant funded by the Korea government (MOTIE) (No. 20134030200360).

References

- Asgari, S.A., Hodgson, P.D., Yang, C., Rolfe, B.F., 2009. Modeling of advanced high strength steels with the realistic microstructure–strength relationships. *Comput. Mater. Sci.* 45, 860–866.
- Cao, Y.P., Lu, J., 2004. A new method to extract the plastic properties of metal materials from an instrumented spherical indentation loading curve. *Acta Mater.* 52, 4023–4032.
- Choi, B.-W., Seo, D.-H., Yoo, J.-Y., Jang, J.-I., 2009a. Predicting macroscopic plastic flow of high-performance, dual-phase steel through spherical nanoindentation on each microphase. *J. Mater. Res.* 24, 816–822.
- Choi, B.W., Seo, D.H., Jang, J.-I., 2009b. A nanoindentation study on the micromechanical characteristics of API X100 pipeline steel. *Met. Mater. Int.* 15, 373–378.
- Choi, I.-C., Yoo, B.-G., Kim, Y.-J., Seok, M.-Y., Wang, Y., Jang, J.-I., 2011. Estimating the stress exponent of nanocrystalline nickel: sharp vs. spherical indentation. *Scr. Mater.* 65, 300–303.
- Chollacoop, N., Ramamurty, U., 2005. Experimental assessment of the representative strains in instrumented sharp indentation. *Scr. Mater.* 53, 247–251.
- Chollacoop, N., Ramamurty, U., 2006. Robustness of the algorithms for extracting plastic properties from the instrumented sharp indentation data. *Mater. Sci. Eng. A* 423, 41–45.
- Davis, J.R., 1998. *Metals Handbook: Desk Edition*, second ed. CRC Press, Boca Raton, FL.
- Eshelby, J.D., 1957. The determination of the elastic field of an ellipsoidal inclusion, and related problems. *Proc. R. Soc. A* 241, 376–396.
- Herbert, E.G., Oliver, W.C., Pharr, G.M., 2006. On the measurement of yield strength by spherical indentation. *Philos. Mag.* 86, 5521–5539.
- Hollomon, J.H., 1945. Tensile deformation. *Trans. AIME* 162, 268–290.
- Hüper, T., Endo, S., Ishikawa, N., Osawa, K., 1999. Effect of volume fraction of constituent phase on the stress–strain relationship of dual phase steels. *ISIJ Int.* 39, 288–294.
- Ishikawa, N., Parks, D.M., Socrate, S., Kurihara, M., 2000. Micromechanical modeling of ferrite–pearlite steels using finite element unit cell models. *ISIJ Int.* 40, 1170–1179.
- Ishikawa, N., Okatsu, M., Endo, S., Kondo, J., 2006a. Design concept and production of high deformability linepipe. In: *Proceedings of IPC, Canada, 10240*.
- Ishikawa, N., Endo, S., Kondo, J., 2006b. High performance UOE linepipes. *JFE Technical Report 7*, pp. 20–26.
- Jang, J.-I., Choi, Y., Lee, J.-S., Lee, Y.-H., Kwon, D., Gao, M., Kania, R., 2005. Application of instrumented indentation technique for enhanced fitness-for-service assessment of pipeline crack. *Int. J. Fract.* 131, 15–33.
- Jang, J.-I., Shim, S., Komazaki, S.-I., Honda, T., 2007. A nanoindentation study on grain-boundary contributions to strengthening and aging degradation mechanism in advanced 12 Cr ferritic steel. *J. Mater. Res.* 22, 175–185.
- Johnson, K.L., 1985. *Contact Mechanics*. Cambridge University Press, Cambridge.
- Kang, S.-K., Kim, Y.-C., Kim, K.-H., Kim, J.-Y., Kwon, D., 2013. Extended expanding cavity model for measurement of flow properties using instrumented spherical indentation. *Int. J. Plast.* 49, 1–15.
- Karlsson, B., Linden, G., 1975. Plastic deformation of ferrite–pearlite structures in steel. *Mater. Sci. Eng. A* 17, 209–219.
- Khan, A.S., Baig, M., Choi, S.-H., Yang, H.-S., Sun, X., 2012. Quasi-static and dynamic responses of advanced high strength steels: experiments and modeling. *Int. J. Plast.* 30–31, 1–17.
- Kim, N.J., Thomas, G., 1981. Effects of morphology on the mechanical behavior of a dual phase Fe/2Si/0.1 C steel. *Metall. Mater. Trans. A* 12, 483–489.
- Koo, J.-Y., Young, M.J., Thomas, G., 1980. On the law of mixtures in dual-phase steels. *Metall. Trans. A* 11, 852–854.
- Lanzillotto, C.A.N., Pickering, F.B., 1982. Structure–property relationships in dual-phase steels. *Mater. Sci. Technol.* 16, 371–382.
- Lim, Y.Y., Chaudhri, M.M., 1999. The effect of the indenter load on the nanohardness of ductile metals: an experimental study on polycrystalline work-hardened and annealed oxygen-free copper. *Philos. Mag.* 79, 2979–3000.
- Lobo, J.A., Geiger, G.H., 1976. Thermodynamics and solubility of carbon in ferrite and ferritic Fe–Mo alloys. *Metall. Trans. A* 7A, 1347–1357.
- Moon, J., Kim, S., Jang, J., Lee, J., Lee, C., 2008. Orowan strengthening effect on the nanoindentation hardness of the ferrite matrix in microalloyed steel. *Mater. Sci. Eng. A* 487, 552–557.
- Mori, T., Tanaka, K., 1973. Average stress in matrix and average elastic energy of materials with misfitting inclusions. *Acta Metall.* 21, 571–574.
- Nix, W.D., Gao, H., 1998. Indentation size effects in crystalline materials: a law for strain gradient plasticity. *J. Mech. Phys. Solids* 46, 411–425.
- Oh, J.-H., Choi, I.-C., Kim, Y.-J., Yoo, B.-G., Jang, J.-I., 2011. Variations in overall- and phase-hardness of a new Ni-based superalloy during isothermal aging. *Mater. Sci. Eng. A* 528, 6121–6127.
- Oliver, W.C., Pharr, G.M., 1992. An improved technique for determining hardness and elastic modulus using load and displacement sensing indentation experiments. *J. Mater. Res.* 7, 1564–1583.
- Oliver, W.C., Pharr, G.M., 2004. Measurement of hardness and elastic modulus by instrumented indentation: advances in understanding and refinements to methodology. *J. Mater. Res.* 19, 3–20.
- Ramazani, A., Mukherjee, K., Prah, U., Bleck, W., 2012. Modelling the effect of microstructural banding on the flow curve behavior of dual-phase (DP) steels. *Comput. Mater. Sci.* 52, 46–54.
- Ramazani, A., Mukherjee, K., Schwedt, A., Goravanchi, P., Prah, U., Bleck, W., 2013a. Quantification of the effect of transformation-induced geometrically necessary dislocations on the flow-curve modeling of dual-phase steels. *Int. J. Plast.* 43, 128–152.
- Ramazani, A., Mukherjee, K., Quade, H., Prah, U., Bleck, W., 2013b. Correlation between 2D and 3D flow curve modeling of DP steels using a microstructure-based RVE approach. *Mater. Sci. Eng. A* 560, 129–139.
- Rudiono, Tomota, Y., 1997. Application of the secant method to prediction of flow curves in multi-microstructure steels. *Acta Mater.* 45, 1923–1929.
- Shim, S., Jang, J.-I., Pharr, G.M., 2008. Extraction of flow properties of single-crystal silicon carbide by nanoindentation and finite element simulation. *Acta Mater.* 56, 3824–3832.
- Sreeranganathan, A., Gokhale, A., Tamirisakandala, S., 2008. Determination of local constitutive properties of titanium alloy matrix in boron-modified titanium alloys using spherical indentation. *Scr. Mater.* 58, 114–117.
- Sun, L., Wagoner, R.H., 2013. Proportional and non-proportional hardening behavior of dual-phase steels. *Int. J. Plast.* 45, 174–187.
- Swadener, J.G., George, E.P., Pharr, G.M., 2002. The correlation of the indentation size effect measured with indenters of various shapes. *J. Mech. Phys. Solids* 50, 681–694.
- Swift, H.W., 1952. Plastic instability under physics of solids. *J. Mech. Phys. Solids* 1, 1–18.
- Tabor, D., 1951. *Hardness of Metals*. Clarendon Press, Oxford.
- Tomota, Y., Kuroki, K., Mori, T., Tamura, I., 1976. Tensile deformation of two-ductile-phase alloys: flow curves of α - γ Fe–Cr–Ni alloys. *Mater. Sci. Eng. A* 24, 85–94.
- Tomota, Y., Umemoto, M., Komatsubara, N., Hiramatsu, A., Nakajima, N., Moriya, A., Watanabe, T., Nanba, S., Anan, G., Kunishige, K., Higo, Y., Miyahara, M., 1992. Prediction of mechanical properties of multi-phase steels based on stress–strain curves. *ISIJ Int.* 32, 343–349.
- Yoo, B.G., Kim, Y.J., Oh, J.H., Ramamurty, U., Jang, J.-I., 2009. On the hardness of shear bands in amorphous alloys. *Scr. Mater.* 61, 951–954.
- Yoo, B.-C., Kim, K.-S., Oh, J.-H., Ramamurty, U., Jang, J.-I., 2010. Room temperature creep in amorphous alloys: influence of initial strain and free volume. *Scr. Mater.* 63, 1205–1208.
- Zhu, L., Lu, J., 2012. Modelling the plastic deformation of nanostructured metals with bimodal grain size distribution. *Int. J. Plast.* 30–31, 166–184.